EDGEWOOD CHEMICAL BIOLOGICAL CENTER

U.S. ARMY RESEARCH, DEVELOPMENT AND ENGINEERING COMMAND

Aberdeen Proving Ground, MD 21010-5424

ECBC-TR-1477

UNIVERSAL RATE MODEL SELECTOR: A METHOD TO QUICKLY FIND THE BEST-FIT KINETIC RATE MODEL FOR AN EXPERIMENTAL RATE PROFILE

Waleed Maswadeh
Richard Vanderbeek
Erik Emmons
Jason Guicheteau
Ashish Tripathi

RESEARCH AND TECHNOLOGY DIRECTORATE

August 2017

U.S. ARMY
RDECOM

Disclaimer

The findings in this report are not to be construed as an official Department of the Army position unless so designated by other authorizing documents.

REPORT DOCUMENTATION PAGE

1. REPORT DATE *(DD-MM-YYYY)*	2. REPORT TYPE	3. DATES COVERED *(From - To)*
XX-08-2017	Final	Mar 2016 – Mar 2017

4. TITLE AND SUBTITLE	5a. CONTRACT NUMBER
Universal Rate Model Selector: A Method to Quickly Find the Best-Fit Kinetic Rate Model for an Experimental Rate Profile	
	5b. GRANT NUMBER
	5c. PROGRAM ELEMENT NUMBER

6. AUTHOR(S)	5d. PROJECT NUMBER
Maswadeh, Waleed; Vanderbeek, Richard; Emmons, Erik; Guicheteau, Jason; and Tripathi, Ashish	
	5e. TASK NUMBER
	5f. WORK UNIT NUMBER

7. PERFORMING ORGANIZATION NAME(S) AND ADDRESS(ES)	8. PERFORMING ORGANIZATION REPORT NUMBER
Director, ECBC, ATTN: RDCB-DRI-S, APG, MD 21010-5424	ECBC-TR-1477

9. SPONSORING / MONITORING AGENCY NAME(S) AND ADDRESS(ES)	10. SPONSOR/MONITOR'S ACRONYM(S)
Defense Threat Reduction Agency, 8725 John J. Kingman Road, MSC 6201, Fort Belvoir, VA 22060-6201	DTRA
	11. SPONSOR/MONITOR'S REPORT NUMBER(S)

12. DISTRIBUTION / AVAILABILITY STATEMENT
Approved for public release: distribution unlimited.

13. SUPPLEMENTARY NOTES

14. ABSTRACT:
Often, a kinetic rate equation does not adequately model an entire set of experimental data points. Traditional kinetic rate models are usually forced onto the experimental points. Traditional algorithmic approaches require additional efforts and processes to find a kinetic rate model that provides a high degree of correlation with experimental data. Furthermore, the use of kinetic rate models does not take into consideration that a set of experimental data points may require more than one type of model to fit the entire data set. That is, different chemical and physical mechanisms may occur during an experimental procedure on an analyte. Herein, we constructed a blueprint (platform) set of graphs that contained eight traditional, widely used kinetic rate model curves as the Universal Rate Model Selector (URMS). Normalized experimental data sets that consisted of different temperatures and pH values for an analyte were overlaid directly onto the blueprint platform (eight kinetic rate curves). Visual observations showed where the normalized data points most closely associated with a particular rate curve(s). No fitting or calculations were performed in the fit between experimental data and the URMS. Instead, a visual analysis was conducted.

15. SUBJECT TERMS

Universal kinetic rate model selector (URMS)	Kinetic modeling	Kinetic data set fitting
Surface-enhanced Raman spectroscopy (SERS)	Biosensor	Degree of correlation

16. SECURITY CLASSIFICATION OF:			17. LIMITATION OF ABSTRACT	18. NUMBER OF PAGES	19a. NAME OF RESPONSIBLE PERSON
a. REPORT	b. ABSTRACT	c. THIS PAGE			Renu B. Rastogi
			UU	32	19b. TELEPHONE NUMBER *(include area code)*
U	U	U			(410) 436-7545

Blank

PREFACE

The work described in this report was started in March 2016 and completed in March 2017.

The use of either trade or manufacturers' names in this report does not constitute an official endorsement of any commercial products. This report may not be cited for purposes of advertisement.

This report has been approved for public release.

Acknowledgments

Blank

CONTENTS

FIGURES

TABLES

UNIVERSAL RATE MODEL SELECTOR: A METHOD
TO QUICKLY FIND THE BEST-FIT KINETIC RATE MODEL
FOR AN EXPERIMENTAL RATE PROFILE

1. INTRODUCTION

A kinetic experiment (e.g., time vs intensity or concentration measurements) requires a kinetic rate model to fit the experimental data points. In the literature, there are many kinetic rate models to choose from (*1, 2*), including the fractional power (*3*), pseudo-first-order (*4*), pseudo-second-order (*5*), Elovich (*6*), Avrami (*7*), and intraparticle diffusion (*6*) rate equations to name a few.

A single fitting algorithm (kinetic rate model) for a reaction does not usually address multiple regions of an experimental rate profile, such as the initial or end (saturation) stages where deviations or discrepancies may be found. Experimental data versus model-fitting discrepancies at the initial stage of a rate profile analysis are common because the independent *y* values are generally located on the steep portion of the kinetic rate decay curve. This is also a concern for the later-stage data points because a greater degree of scatter is common. Different chemical and physical mechanisms may occur during an experiment to cause these differences. The fitting algorithm also provides the best-fit parameters (degree of correlation) to produce a minimum error-squared value. As the number of fitting parameters in a rate model increases, a higher degree of correlation is usually observed. However, over-fitting may occur, and the fitting parameter(s) may lose meaning or association.

In general, a kinetic rate model can be divided and classified according to the number of rate constants. It should be noted that the majority of traditional rate models need to be converted into time versus relative intensity (or relative concentration or percent conversion) so the values can be directly compared.

The concept of forcing or fitting a particular kinetic rate model onto a complete data set may overlook salient or significant alternate trends in a portion of the complete record of data. Herein, we constructed a blueprint (platform) set of graphs that contains eight traditional, widely used kinetic rate model curves as the platform for the Universal Rate Model Selector (URMS). The URMS was tested using surface-enhanced Raman spectroscopy (SERS) of thiophenol adsorption onto a gold surface. SERS experimental data sets of thiophenol, which consisted of different experimental conditions and parameters (*8*), were overlaid directly onto the URMS blueprint platform (eight kinetic rate curves). A visual observation showed where the normalized experimental data points most closely associated with a particular rate curve. No fitting or calculations were performed in the fit between experimental data and the URMS. Instead, a visual analysis was conducted. High degrees of correlation were observed with the normalized experimental data points and selected URMS curves. Therefore, the experimental data points were used to select the rate model curves that showed the closest association.

2.   MATERIALS AND METHODS

Experimental thiophenol rate profiles (time vs SERS signal) at four different pH values and six different temperatures (total of 25 rate profiles) were acquired using commercial nanostructured gold SERS substrates (*8*). Thiophenol is a model system for adsorption rate studies of molecules on noble metal surfaces due to the strong affinity of the –SH group for these metals. Figure 1 shows all 25 experimental thiophenol rate profiles at four different pH values (four panels in Figure 1) and at different temperatures. There are six rate profiles at pH 2 and temperatures of 1.7, 13.7, 25.2, 34, 42.5, and 54.1 °C. There are six rate profiles at pH 4 at temperatures of 0.7, 3.7, 13.3, 26.4, 42.6, and 54.5 °C. There are six rate profiles at pH 6 at temperatures of 1.5, 12.8, 25.7, 34.2, 42.5, and 55.3 °C. There are seven rate profiles at pH 10 at temperatures of 1.7, 3.4, 12.5, 25.2, 32.6, 42.8, and 53.7 °C. Different rate profiles have different maximum intensities, which may be attributed to the variations on the SERS substrate, Klarite, slides (Renishaw Diagnostics Limited, Glasgow, U.K.). Intensity spikes may be due to (1) variations between Klarite slides, (2) system performance over a period of time, (3) pH control, (4) temperature control, and (5) environmental noise.
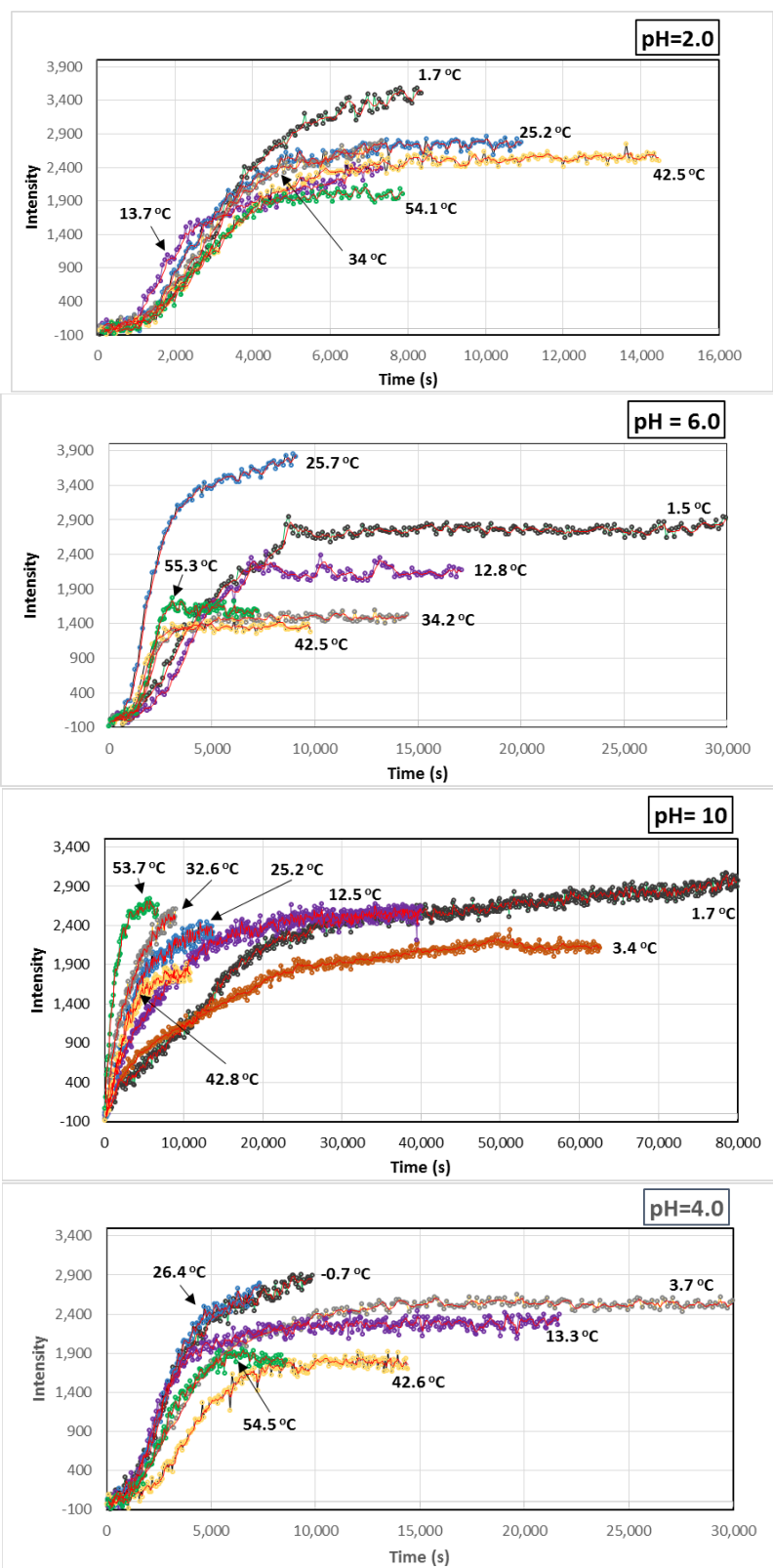
Figure 1. Twenty-five experimental thiophenol rate profiles at pH 2, 4, 6, and 10 and at various temperatures.

3.   RESULTS AND DISCUSSION

3.1   Calculation of Effective Intensity

The first step was to scale and normalize the SERS intensity values and convert them to experimental relative intensities ($R_{exp} = 0–1$) using the experimental minimum and maximum intensity, I_{min} and I_{max}, respectively, as follows:

$$R_{exp} = (I - I_{min})/(I_{max} - I_{min}) \tag{1}$$

where R_{exp} is the experimental relative intensity, based on the experimental maximum intensity.

The question then arose as to how to scale the intensity values (I) and determine the proper I_{min} and I_{max} values. For example, the I_{max} value or the average maximum intensity value at the saturation or plateau region could be used (Figure 2). Equation 1 was modified as follows:

$$R_p = R_{adj} \times R_{exp} \tag{2}$$

where R_p is the predicted relative intensity, based on the predicted maximum intensity, I_{maxp}, and R_{adj} is the adjusted I_{max} intensity factor

$$R_{adj} = (I_{max} - I_{min})/(I_{maxp} - I_{min}) \tag{3}$$
$$= (I_{max} - I_{min})/(I_{max} + \Delta I - I_{min})$$

and

$$I_{maxp} = I_{max} + \Delta I \tag{4}$$

R_{adj} is necessary because this term takes into consideration whether an experiment was performed to completion (into the plateau or saturation phase, e.g., Figure 1 at pH 2, 42.5 °C and at pH 6, 1.5 °C) or whether the experiment was not allowed to proceed to completion. If an experiment is stopped before it reaches the saturation or plateau phase, then that I_{max} (apparent maximum intensity) is actually lower than the true maximum (predicted maximum intensity). Therefore, the ΔI term is the difference between I_{maxp} and I_{max}. Examples of this situation are shown in Figure 1 at pH 2, 1.7 °C and at pH 6, 25.7 °C. Therefore, R_p at time (t) is the adjusted R_{adj} intensity multiplied by R_{exp}.

Figure 2. Experimental rate profiles at pH 6. The I_{max} and average maximum intensity values are indicated with arrows.

Figure 3 shows all 25 experimental thiophenol rate profiles at pH 2, 4, 6, and 10 and at different temperatures after the intensity values were converted to effective intensities (R_p) using eq 2. The rate profiles at pH 10 (Figure 3, bottom panel) show more temperature dependency than the rate profiles at the other pH values. Rate profiles at pH 2 show the least temperature dependency, but the profile at 13.7 °C is questionable. Rate profiles at pH 6 show strong temperature dependency at temperatures 12.8 and 1.5 °C, and rate profiles at pH 4 show some degree of temperature dependency.
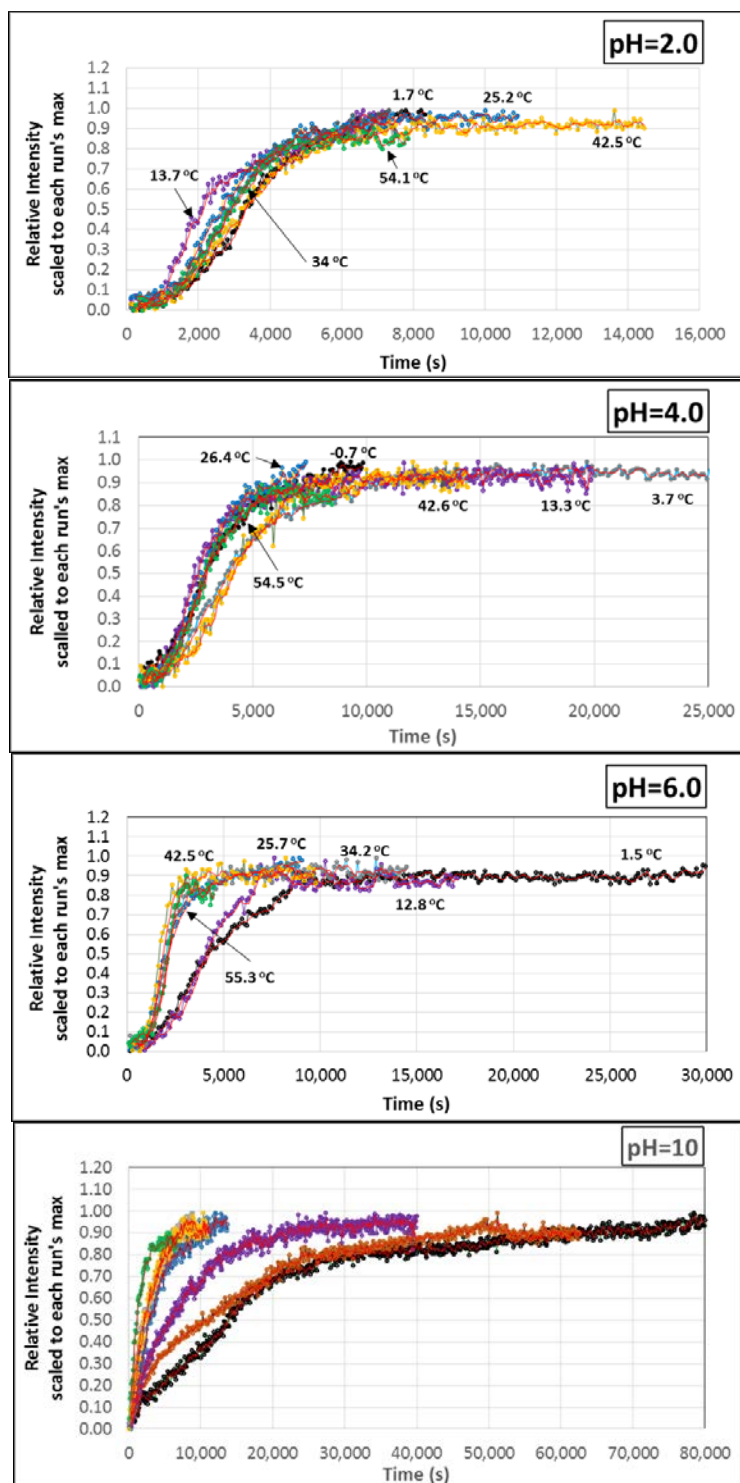
Figure 3. Twenty-five experimental thiophenol rate profiles at pH 2, 4, 6, and 10 and at various temperatures after the intensity values were converted to effective intensities using eq 2.

3.2 Kinetic Rate Models

Metal–organic complex mechanisms of adsorption often involve a chemical reaction between functional groups on a sorbent surface with the metal ions, thus forming metal–organic complexes. This produces a cation-exchange reaction due to the high cation-exchange capacity of the sorbent. In addition, other mechanisms may be involved including mass-transport processes such as transport in the bulk of the liquid phase, diffusion across the liquid film near the surface, and diffusion in macro- or micropores. Adsorption kinetics have been extensively studied. Usually, the adsorption rate is very rapid at the beginning of the process and then becomes slower as equilibrium is approached. Such kinetics are often described by a first-order kinetic reaction (*9–11*) and are sometimes interpreted as a combination of two or three different mechanisms (*12–18*). McKay and Allen (*19, 20*) studied the sorption of dyes onto peat and developed mass-transport diffusion models that were used successfully to predict the dye concentration versus time-decay curves.

Table 1 shows some of the common kinetic rate models with one rate constant that are found in the literature (*7, 21, 22*). Table 2 shows some of the common kinetic rate models with two rate constants that are found in literature (*1–7, 21, 22*).

Table 1. Kinetic Rate Models with One Rate Constant

No.	Name	Rate Equation	1st t_{50}	2nd t_{50}
1	First-order model • Film-diffusion model, • Mass transfer rate or linear driving force (LDF), and • Pseudo-first-order model	$\ln(1 - R_p) = -(k_n t)$ $\ln(1 - R_p) = -(at)$	$E_1/RT =$ $\ln(t_{50}) - \ln[-\ln(0.5)]$	$\ln(1 - R_p) =$ $(t/t_{50})\ln(0.5)$
2	Second-order model Pseudo-second-order model	$[1/(1 - R_p)] =$ $1 + (kt)I_{max}$	$E_1/RT =$ $\ln(t_{50}) - \ln[(0.5^{-1} - 1)]$	$(1 - R_p)^{-1} =$ $1 + (t/t_{50}) [0.5^{-1} - 1]$
3	nth-order model	$(1 - R_p)^{(1-n)} =$ $1 + (k_n t)$ $(n - 1) I_{max}$	$E_1/RT =$ $\ln(t_{50}) -$ $\ln[(0.5^{(1-n)} - 1)/(n - 1)]$	$(1 - R_p)^{(1-n)} =$ $1 + (t/t_{50}) [0.5^{(1-n)} - 1]$
4	Film diffusion model, first-order model (Dumwald–Wagner)	$\ln(1 - R_p^2) =$ $-(k_f t)$	$E_1/RT = \ln(t_{50})$ $- \ln[-\ln(1 - 0.5^2)]$	$\ln(1 - R_p^2) =$ $(t/t_{50})\ln(1 - 0.5^2)$

(table continued)

Table 1. Kinetic Rate Models with One Rate Constant (Continued)

No.	Name	Rate Equation	1st t_{50}	2nd t_{50}
5	First-order autocatalytic reaction model	$R_p + \alpha =$ $[1 + \alpha]/$ $[1 + (1/\alpha)e^{-(kt)(\beta)}]$	$E_1/RT = \ln(t_{50}) -$ $\ln[-\ln(0.5\alpha)/(0.5 + \alpha)]$	$\ln[\alpha(1 - R_p)/(R_p+\alpha)] =$ $(t/t_{50})\ln[\alpha(1 - 0.5)/$ $(0.5 + \alpha)]$
6	Avrami rate model	$\ln(1 - R_p) =$ $-(kt^n)$	$E_1/RT =$ $n\ln(t_{50}) - \ln[-\ln(0.5)]$	$\ln(1 - R_p) =$ $(t/t_{50})^n \ln(0.5)$
Nonconverging Kinetic Rate Models ($R \rightarrow \infty$ when $t \rightarrow \infty$)				
7	Fractional power model	$R_p = (kt^b)$	$E_1/RT =$ $b\ln(t_{50}) - \ln(0.5)$	$R_p/0.5 = (t/t_{50})^b$
8	Intraparticle diffusion model (Weber–Morris)	$R_p \times I_{max} =$ $C_d + k_d\, t^{0.5}$	$E_1/RT =$ $0.5\ln(t_{50}) -$ $\ln(0.5I_{max} - C_d)$	$(R_p - C_d/I_{max}) =$ $(t/t_{50})^{0.5}\,(0.5 - C_d/I_{max})$
9	Bioadsorption: Elovich model	$R_p = \ln(1 +$ $a_e b_e t)/(b_e I_{max})$	$E_1/RT =$ $\ln(t_{50}) - \ln[(e^{0.5bI}$ $- 1)/b_e)]$	When $abt_{50} >> 1$ $R_p - 0.5 =$ $\ln(t/t_{50})/(b_e I_{max})$

where

t_{50} is time when the reaction reaches a relative intensity of 0.5; k is rate constant; t is time; R is ideal gas constant; T is temperature; a is mass rate diffusion rate or LDF effective mass transfer coefficient; E_1 is activation energy associated with rate constant k_1; k_f is film diffusion constant; α is catalyst ratio equal to I_0/I_{max}; $\beta = (1 + \alpha)\,I_{max}$; n is a constant; b is a constant with $b < 1$; k_d is rate of intraparticle diffusion-controlled adsorption constant; C_d is 0 when diffusion is limiting step; a_e is the initial adsorption rate (mg/g·h); and b_e is desorption constant (g/mg).

Table 2. Kinetic Rate Models with Two Rate Constants

No.	Name	Rate Equation	2nd t_{50}
1	Homogeneous catalytic reaction model	$\ln(1 - R_p) = -(k_1 + k_2 S_2)t$ $\ln(1 - R_p) = -(k_{obs}t)$	$\ln(1 - R_p) = (t/t_{50})\ln(0.5)$
2	Shifting order model 1: Low to high	$-\ln(1 - R_p) + k_2 I_{max} R_p = (k_1 t)$	$k_2 I_{max} - \ln(1 - R_p)/R_p = (\alpha_{s1})(t/t_{50})/R_p$
3	Shifting order model 2: High to low	$\ln(\alpha_{s2}/[\alpha_{s2} - k_2 I_{max} R_p]) = (k_2 t)$	$\ln(1 - k_2 I_{max} R_p/\alpha_{s2}) = (t/t_{50})\ln(1 - 0.5 k_2 I_{max}/\alpha_{s2})$
4	Double exponential model (DEM) (Wilezak–Keinath), two adsorption sites (slow, rapid)	$(1 - R_p) = a_1 e^{-k_1 t} + (1 - a_1)e^{-k_2 t}$	NA
5	Monomolecular consecutive model OR In-series reaction ($n = 2$) model	$(1 - R_p) = \alpha e^{-k_1 t} + (1 - \alpha)e^{-k_2 t}$	NA

where
S is available sites (S_2 is type 2 sites); k_{obs} is observed (effective) rate constant; NA is not applicable.
$k_{obs} = k_1 + k_2 S_2$; $\alpha_{s1} = 0.5 k_2 - \ln(0.5)/I_{max}$; $\alpha_{s2} = k_1 + k_2 I_{max}$; a_1 = fraction of site; $\alpha = k_2/(k_2 - k_1)$

3.3   Universal Kinetic Rate Platform Development

Kinetic rate models range from pure chemical reactions to mass transfer (diffusion) (Tables 1 and 2). The rate equations in Tables 1 and 2 were converted to be independent of the time, intensity, temperature, and activation energy parameters. This new approach offers a unique single curve for each rate model equation. In this format, there is no need to obtain or evaluate kinetic rate constants or mechanisms. The experimental data can be mapped visually onto the transformed rate models that provide a best fit. The fit between the data points and the model curves requires no assumptions, calculations, or prior information about the experimental conditions.

All rate models in Tables 1 and 2 are in the time and intensity domains, and the time parameter needs to be converted into dimensionless units. To do that, we used the t/t_{50} parameter. The t_{50} is the time when the reaction reaches a relative intensity of 0.5 ($R_p = 0.5$), or the time t when the reaction reaches 50% conversion. There are two approaches for constructing the t_{50}, as shown in Table 1. The first t_{50} approach (1st t_{50}) was applied to the rate models in Table 1, and the results are shown under the 1st t_{50} column in Table 1. Table 1 shows a general linear relationship between $\ln(t_{50})$ and $1/T$, where the slope equals E_1/nR and $n = 0.5$ for rate

model no. 8 (Weber–Morris), n is constant for rate model no. 6 (Avrami model), and $n = 1$ for all other models.

The 1st t_{50} approach is a convenient model used to produce a rough estimate on the observed E_1/R values from the experimental rate profiles at different temperatures. However, the 1st t_{50} approach is dependent on temperature and E_1/R.

The second t_{50} approach (2nd t_{50}) was applied to the rate models in Table 1. Table 1 shows that $(t/t_{50})^n$ is a function (f) of R_p or f(R_p) with $n = 0.5$ for rate model no. 8; n is constant for rate model no. 6, and $n = 1$ for all other models. The 2nd t_{50} approach appears to be superior to the 1st t_{50} approach because the 2nd t_{50} approach converts the traditional kinetic rate models so that they are independent of time, intensity, temperature, rate constant, and activation energy.

Table 1 shows that each kinetic rate model has a single, unique curve in the (t/t_{50}) versus R_p plot. Because $(t/t_{50}) = 1$ is an inversion point in the kinetic rate models, R_p was replaced with $R_p(1 - R_p)$ to show the initial stage and the later (close-to-completion) stage curvatures for each rate model. The kinetic rate curves generated by (t/t_{50}) on the x axis and $R_p(1 - R_p)$ on the y axis become the URMS platform.

Results from the rate models in Table 2 were placed into the 2nd t_{50} approach as listed.

Figure 4 shows the URMS platform where the kinetic rate models have no dependence on temperature, time, and E_1/R. The four different temperatures (1.7, 10, 25, and 43 °C) produced identical curves in the URMS platform for each respective rate model, which showed kinetic rate model temperature independence. For the one rate constant models (Table 2), there was no dependency on E_1/R. This was also true for the two rate constant kinetic models when $|\Delta E_{12}|/R$ was kept constant. $\Delta E_{12} = E_2 - E_1$, where E_2 and E_1 are the activation energies associated with rate constants k_2 and k_1, respectively.
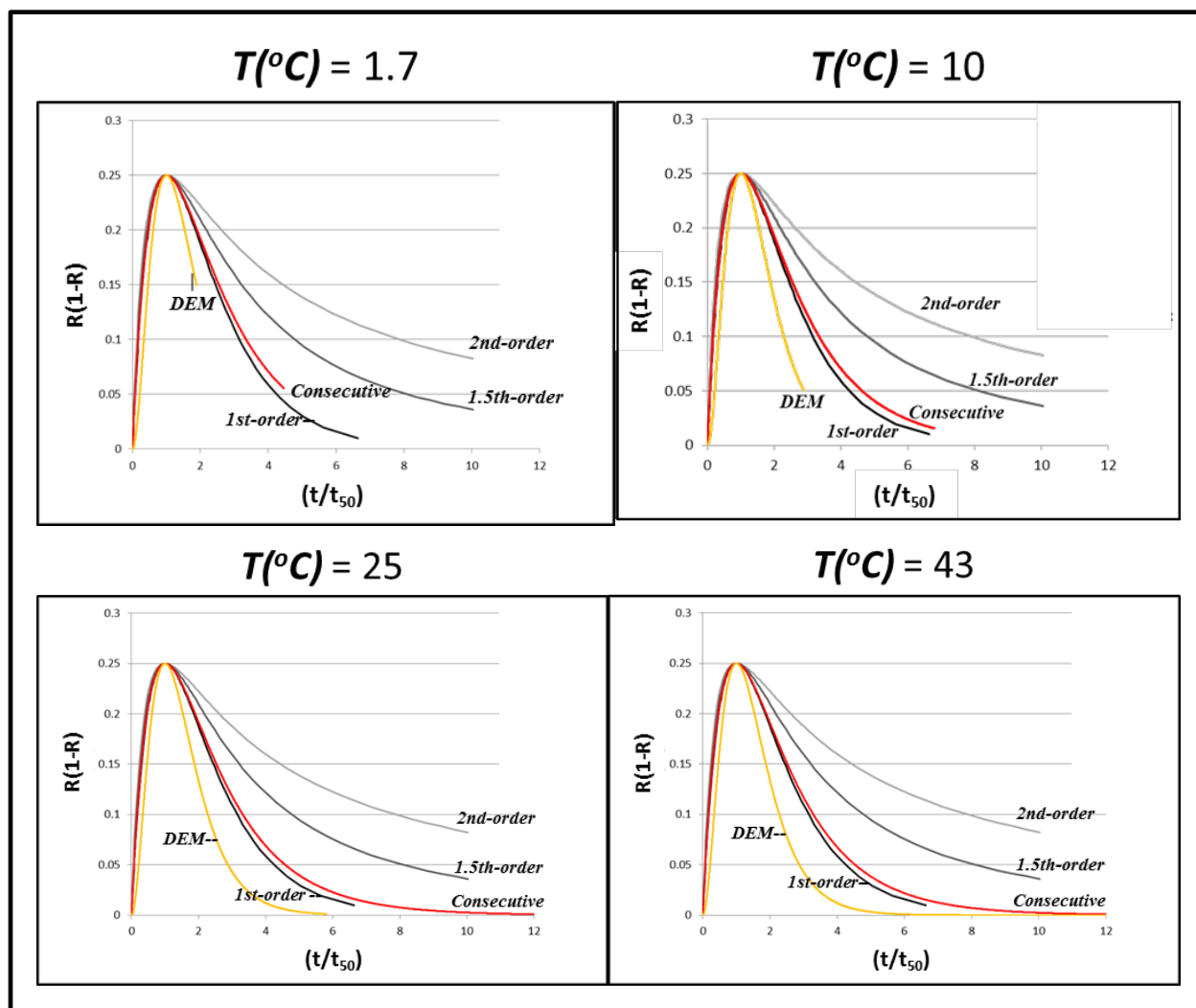
Figure 4. One rate constant models in the URMS platform that are independent of temperature, time, and E_1/R.

Figures 5 and 6 show the effects of changing the E_1/R and $|\Delta E_{12}|/R$ values, respectively, for the two rate constant kinetic models. Figure 5 shows identical plots for the URMS platform when $|\Delta E_{12}|/R$ values are kept constant ($|\Delta E_{12}|/R = 55$) while changing the E_1/R values. But when $|\Delta E_{12}|/R$ increases (Figure 6), the curve broadens significantly on the right side of the plot ($t/t_{50} = 1$), regardless of whether E_1/R is held constant or not. Each $|\Delta E_{12}|/R$ value produces a unique curve in the URMS platform. The percentage of ($|\Delta E_{12}|/E_1$) appears to strongly affect the later stage degree of widening, especially above 50%.

Figure 6 shows a general trend on URMS curves containing two rate constants. For each $|\Delta E_{12}|/E_1$ value, there exists a unique URMS curve with the two rate constant kinetic rate model.

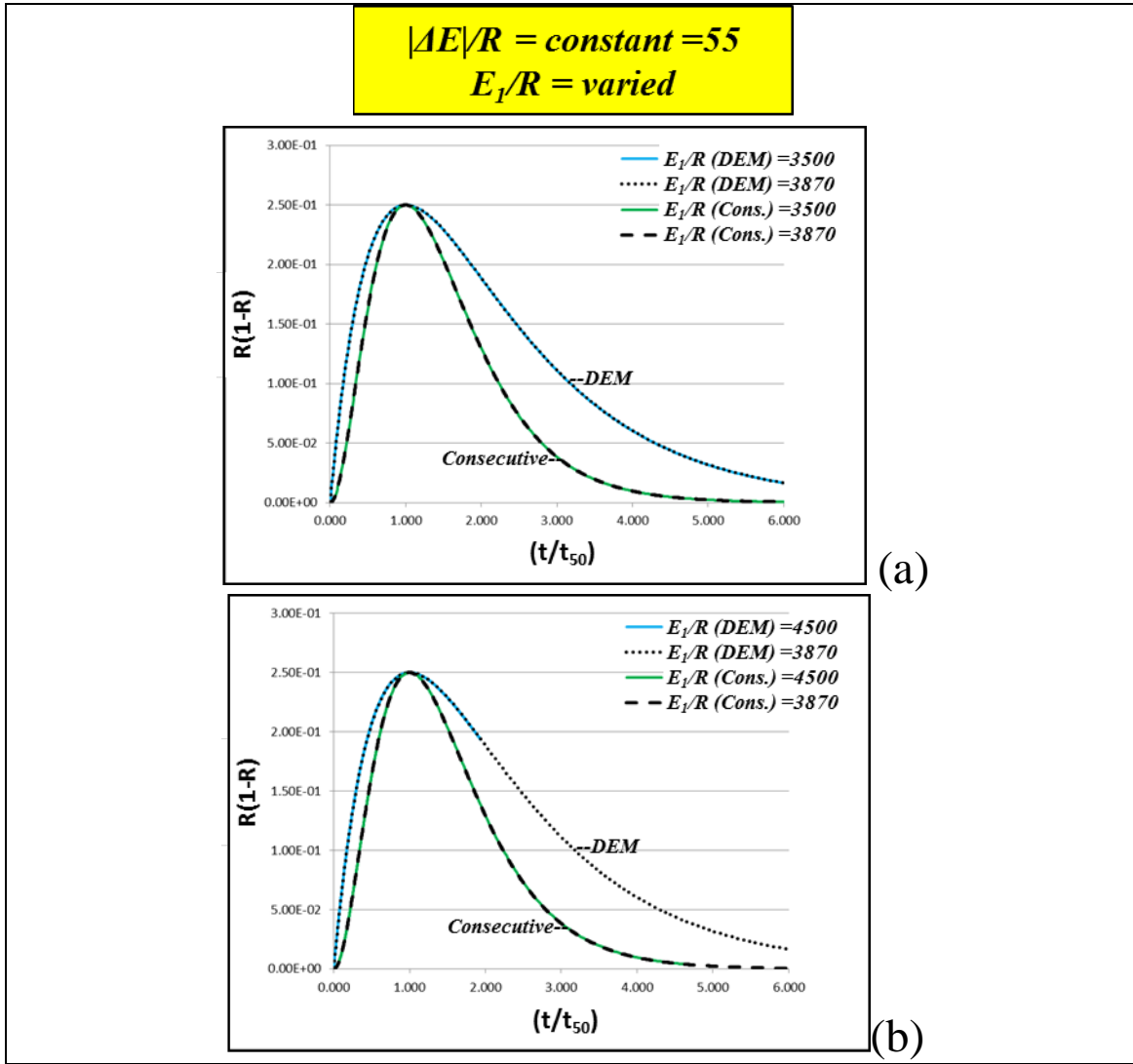Figure 5. The E_1/R values of the blue and green curves were changed from 3500 (a) to 4500 (b). The dotted and dashed curves are reference curves with fixed E_1/R values of 3870. It is clear that the blue and green curves did not change as compared with the reference curves when $|\Delta E_{12}|/R$ values were kept constant (55), while the E_1/R values were changed. Cons., consecutive (in-series) rate model.
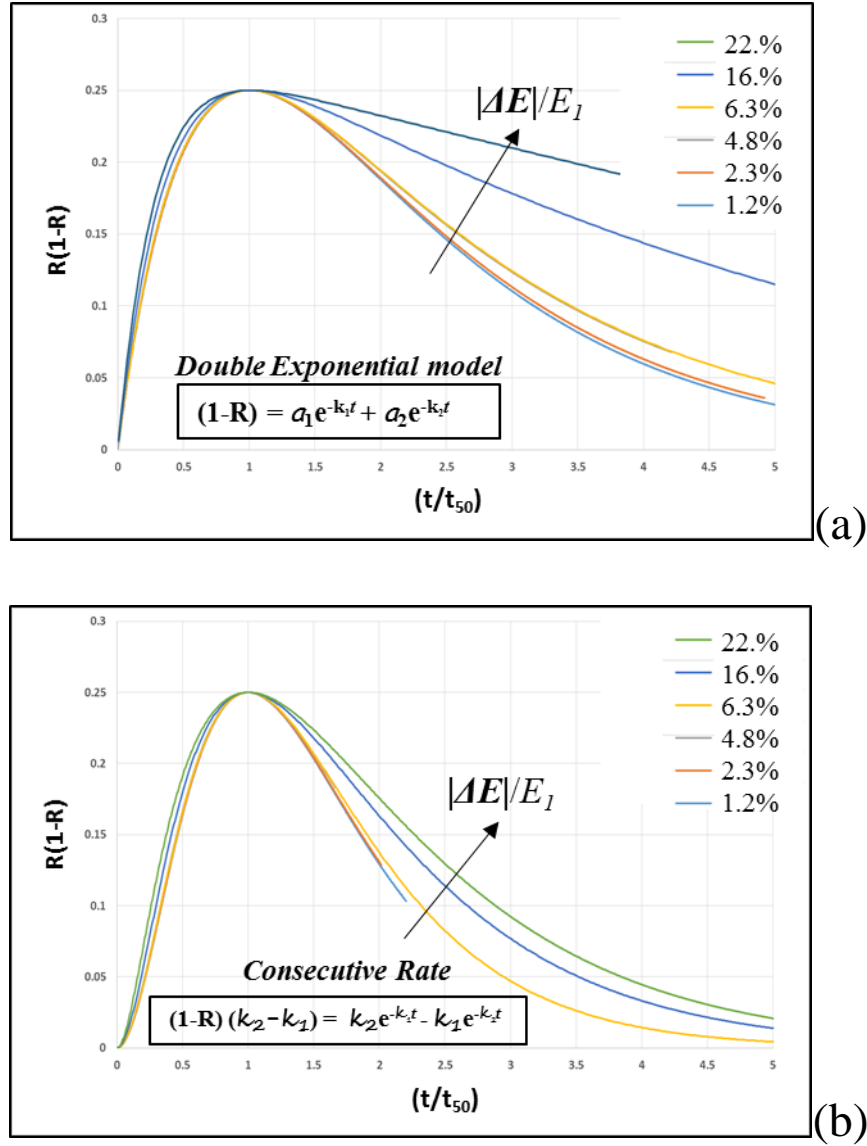
Figure 6. Effects of changing $|\Delta E_{12}|/R$ values on the two rate constant kinetic rate models in the URMS platform. When $|\Delta E_{12}|/R$ was increased, the DEM (a) showed more significant widening than the Cons. (b) for the same ($|\Delta E_{12}|/E_1$) percentage.

Figure 7 shows the URMS curves with nth-order rate models at $n = 0.25$, 1, and 2; homogeneous catalytic rate model (pseudo-first-order); DEM at two different $|\Delta E_{12}|$ values (55 and 155); and consecutive rate models at two different $|\Delta E_{12}|$ values (55 and 155). We chose these rate models because they represent the commonly used traditional kinetic rate models found in the literature (*3–11, 21, 22*). $R_p = 0–1$ when the time (t) goes from 0 to ∞.

Figure 7. URMS models at $n = 0.25$, 1, and 2. Also shown are the DEM and Cons. at selected ΔE_1 values.

We tested the URMS platform (Figure 7) with experimental SERS thiophenol rate profiles at pH 10 (Figure 8). The six experimental rate profiles at 1.7, 12.5, 25.2, 32.6, 42.8, and 53.7 °C were evaluated visually to see which rate model had the highest degree of correlation with the experimental data points. The URMS platform offer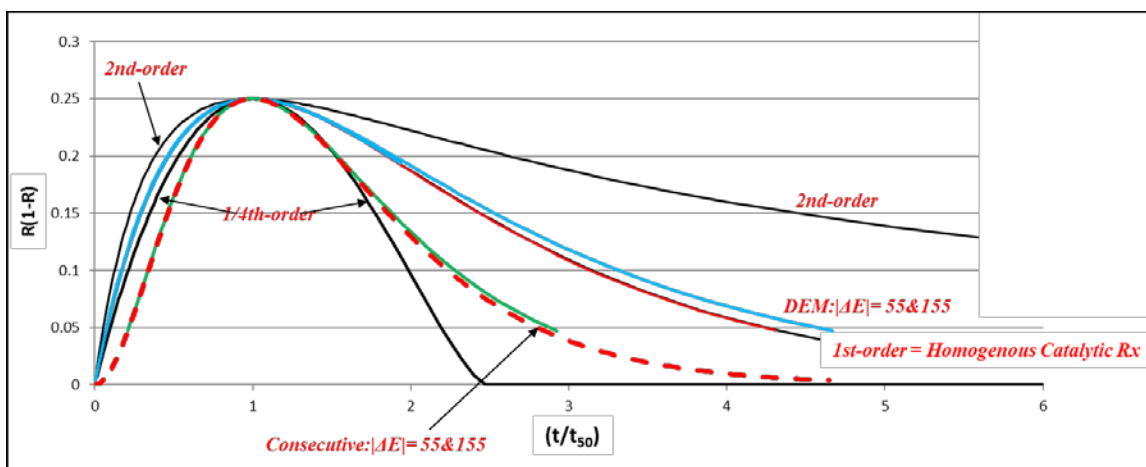s a unique type of evaluation, which is a comparison of each experimental rate profile with any changes with varying temperatures. Figure 8 shows that a first-order rate model is generally a best fit for the experimental points. This behavior was also noted by Biggs and colleagues (*23*), where the SERS peak growth appeared to follow the time-dependent Langmuir kinetics (first-order rate model).

There were some deviations from a first-order rate model at the later stage when $t/t_{50} > 2.5$. Was this because (1) the R_p values were very similar to R_{exp} or (2) there was a change in the mechanism from a first- to second-order reaction rate model? Biggs and colleagues (*23*) noted that the DEM behavior was consistent with a gradual reordering of the adsorbed layer as the surface approached saturation coverage. This is a phenomenon previously observed in benzylthiol and other organothiol adsorption studies (*24–26*).

Also, there was a change in the initial stage of the profiles when $t/t_{50} < 1.0$. Some of the experimental data points were closer to a second-order rate model, whereas other data points were closer to a first-order model.
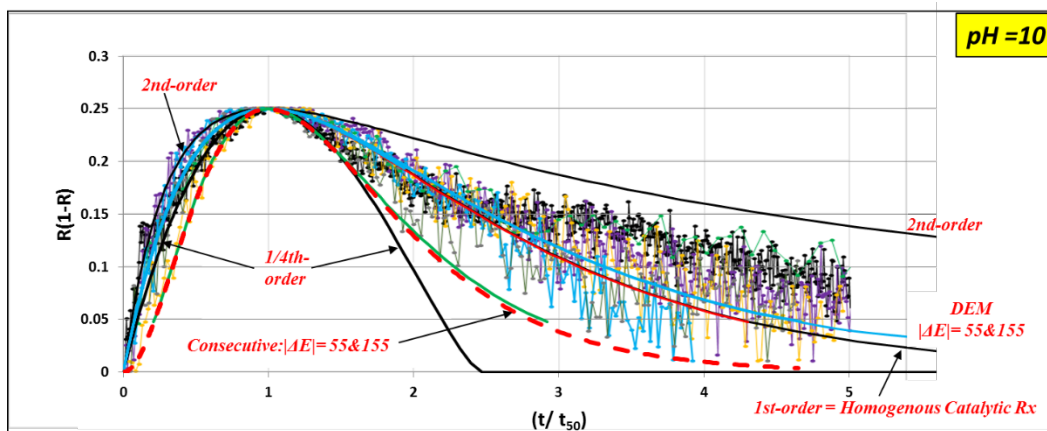
Figure 8. The rate model that best fits the experimental data is
a first-order or homogeneous catalytic reaction.

We also tested the URMS platform in Figure 7 with a second set of experimental SERS thiophenol rate profiles at pH 6 (Figure 9). The six experimental rate profiles at 1.5, 12.8, 25.7, 34.2, 42.5, and 55.3 °C were evaluated visually to see which rate model had the highest degree of correlation with the experimental data points. Figure 9 shows that no rate model adequately fit the experimental data points. The consecutive rate model showed a low correlation.
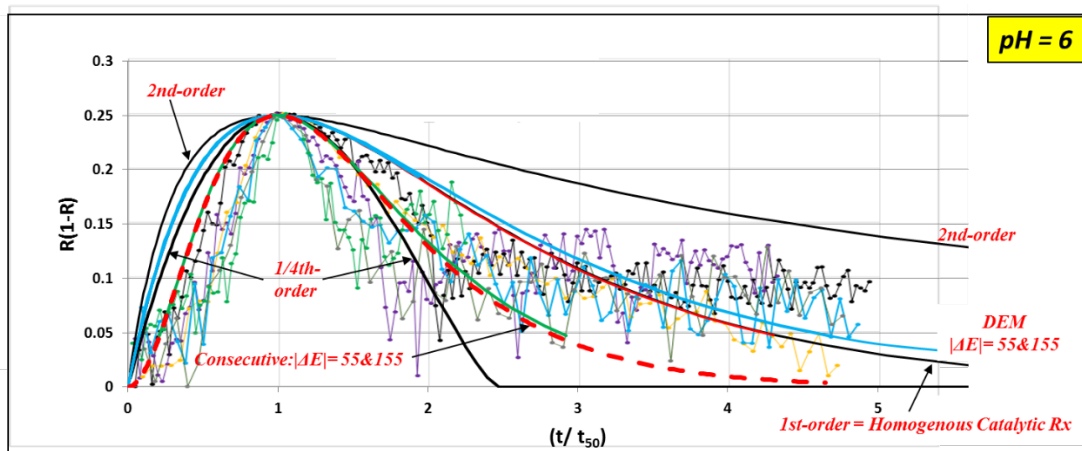
Figure 9. No single rate model appears to fit the experimental data.

We tested the URMS platform in Figure 7 with a third set of experimental SERS thiophenol rate profiles at pH 4 (Figure 10). Figure 10 shows that the six experimental rate profiles at –0.7, 3.7, 13.3, 26.4, 42.6, and 54.5 °C were evaluated visually for the rate model that had the highest degree of correlation with the experimental data points. No single rate model provides an adequate fit to the experimental data points. The consecutive rate model had a substantially low degree of correlation with the data points. It is interesting that Figures 9 and 10 showed similar experimental data point profiles. This was significant because at pH 10, the rate

15

profiles were different from those at pH 6 and below. This behavior was also explained by Biggs and colleagues (*23*), where the growth in intensity of the 422 cm^{-1} peak was best described by the DEM two rate constant model. The 422 cm^{-1} curve deviation from first-order Langmuir kinetics was likely related to its strong dependence on the α_{zz} tensor value, that is, its electromagnetic enhancement was very sensitive to surface-layer orientation (*27*).
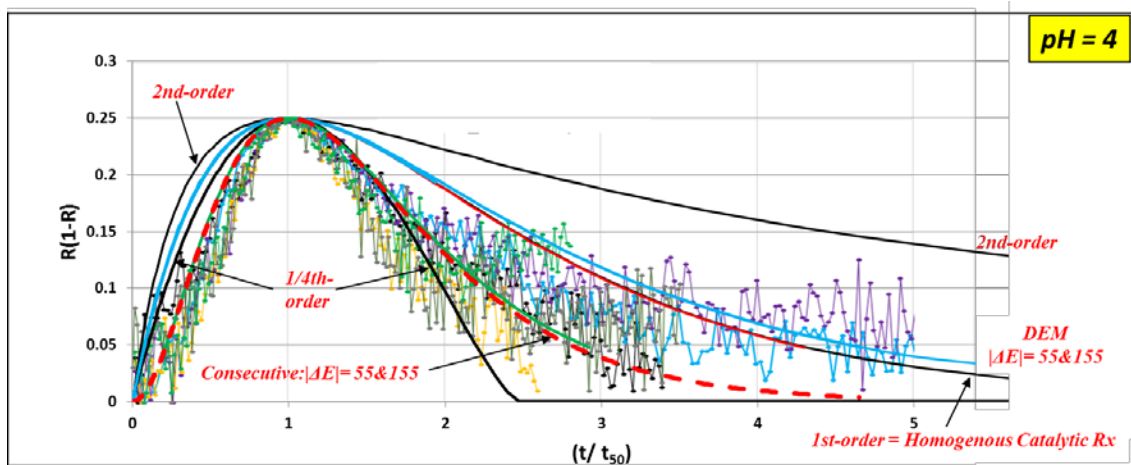
Figure 10. A comparison of the rate models with the experimental data at pH 4.

We tested the URMS platform in Figure 7 with a fourth set of experimental SERS thiophenol rate profiles at pH 2 (Figure 11). The six experimental rate profiles at 1.7, 13.7, 25.2, 34, 42.5, and 54.1 °C were evaluated visually to see which rate model had the highest degree of correlation with the experimental data points. Figure 11 shows that no combination of rate models adequately fits the experimental data points.
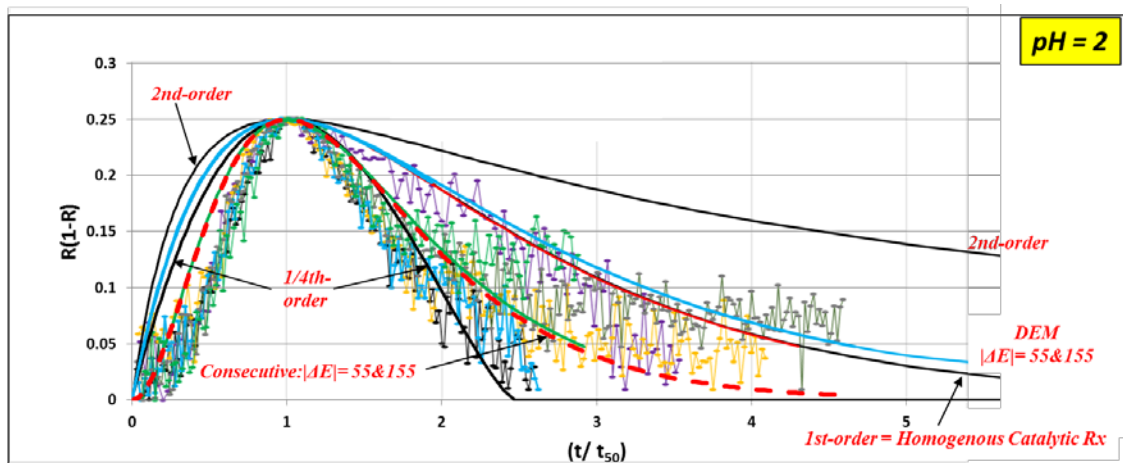

Figure 11. A comparison of the rate models with the experimental data at pH 2.

It is significant to note that from pH 10 to 2 (Figures 8–11), the experimental profiles showed a tendency to become narrower. Furthermore, the initial stage of the experimental profiles ($0 < t/t_{50} < 1$) showed a delay in the initial rise as the pH value decreased.

4.   CONCLUSIONS

The URMS presents a fast and easy way for a visual analysis of complex experimental rate profiles that consist of many data points obtained at different operating conditions (temperature and pH values). The URMS platform helps to visually evaluate the experimental rate profiles to determine the best kinetic model that exhibits a relatively high degree of correlation. Any changes that may occur during the initial and later stages of experimentation (saturation), as well as how the rate profile changes with operating conditions such as temperature and pH, are easily observed with the URMS. The kinetic rate model equations were solved without considering the major parameters such as temperature, rate constant, activation energy, time, and intensity.

Future efforts will address rate models with equal to or greater than three rate constants (three activation energies; E_1, E_2, and E_3). URMS models will be devised for each pair of $|\Delta E_{12}|/E_1$, $|\Delta E_{13}|/E_1$, and $|\Delta E_{23}|/E_2$ values. $\Delta E_{13} = E_3 - E_1$ and $\Delta E_{23} = E_3 - E_2$, where E_3 is the activation energy associated with rate constant k_3.

Blank

LITERATURE CITED

1. Huang, P.M.; Li, Y.L.; Sumner, M.E. *Handbook of Soil Sciences: Properties and Processes*, 2nd ed.; CRC Press: Boca Raton, FL, 2011.

2. Turanyi, T.; Tomlin, A.S. *Analysis of Kinetic Reaction Mechanisms*; Springer Publishing Company: Berlin, 2014.

3. Das, D.; Vimala, R.; Das, N. Biosorption of Zn(II) onto Pleurotus Platypus: 5-Level Box–Behnken Design, Equilibrium, Kinetic and Regeneration Studies. *Ecol. Eng.* **2014,** *64*, 136–141.

4. Tseng, R.L.; Wu, P.-H.; Wu, F.-C.; Juang, R.-S. A Convenient Method to Determine Kinetic Parameters of Adsorption Processes by Nonlinear Regression of Pseudo-*n*th-order Equation. *Chem. Eng. J.* **2014,** *237*, 153–161.

5. Ho, Y.-S. Using of Pseudo-Second-Order Model in Adsorption. *Environ. Sci. Pollut. Res.* **2014,** *21* (11), 7234–7235.

6. Viegas, R.M.; Campinas, M.; Costa, H.; Rosa M.J. How Do the HSDM and Boyd's Model Compare for Estimating Intraparticle Diffusion Coefficients in Adsorption Processes. *Adsorption* **2014,** *20* (5–6), 737–746.

7. DaSilva, R.A.R.; Guerra, D.J.L. Applications of Brazilian Illite–Kaolinite in Natural and Intercalated Forms as Adsorbents to Removal of Zinc from Aqueous Solutions: Kinetic and Thermodynamic Studies. *J. Chil. Chem. Soc.* **2013,** *58* (2), 1678–1683.

8. Tripathi, A.; Emmons, E.D.; Christesen, S.D.; Fountain, A.W., III; Guicheteau, J.A. Kinetics and Reaction Mechanisms of Thiophenol Adsorption on Gold Studied by Surface-Enhanced Raman Spectroscopy. *J. Phys. Chem. C* **2013,** *117* (44), 22834–22842.

9. Panday, K.K.; Prasad, G.; Singh, V.N. Copper(II) Removal from Aqueous Solutions by Fly Ash. *Water Res.* **1985,** *19* (7), 869–873.

10. Periasamy, K.; Namasivayam, C. Removal of Copper(II) by Adsorption onto Peanut Hull Carbon from Water and Copper Plating Industry Wastewater. *Chemosphere* **1996,** *32* (4), 769–789.

11. Namasivayam, C.; Kadirvelu, K. Agricultural Solid Wastes for the Removal of Heavy Metals: Adsorption of Cu(II) by Coirpith Carbon. *Chemosphere* **1997,** *34* (2), 377–399.

12. Sarkar, D.; Chattoraj, D.K. Activation Parameters for Kinetics of Protein Adsorption at Silica Water Interface. *J. Colloid Interface Sci.* **1993,** *157* (1), 219–226.

13. Taylor, R.W.; Hassan, K.; Mehadi, A.A.; Shuford, J.W. Kinetics of Zinc Sorption by Soils. *Commun. Soil Sci. Plant Anal.* **1995,** *26* (11–12), 1761–1771.

14. Varshney, K.G.; Khan, A.A.; Gupta, U.; Maheshwari, S.M. Kinetics of Adsorption of Phosphamidon on Antimony (V) Phosphate Cation Exchanger: Evaluation of the Order of Reaction and Some Physical Parameters. *Colloids Surf. A – Physicochem. Eng. Asp.* **1996,** *113* (1–2), 19–23.

15. Singh, D.B.; Prasad, G.; Rupainwar, D.C. Adsorption Technique for the Treatment of As(V)-Rich Effluents. *Colloids Surf. A – Physicochem. Eng. Asp.* **1996**a, *111* (1–2), 49–56.

16.   Singh, J.; Huang, P.M.; Hammer, U.T.; Liaw, W.K. Influence of Citric Acid and Glycine on the Adsorption of Mercury(II) by Kaolinite under Various pH Conditions. *Clays Clay Miner.* **1996**b, *44* (1), 41–48.

17.   Atun, G.; Sismanoglu, T.J. Adsorption of 4,4-Iso Propylidene Diphenol and Diphenylolpropane 4,4 Dioxyaceticacid from Aqueous Solution on Kaolinite *J. Environ. Sci. Health A Tox. Hazard. Subst. Environ. Eng.* **1996**, *31* (8), 2055–2069.

18.   Comber, S.D.W.; Gardner, M.J.; Gunn, A.M.; Whalley, C. Kinetics of Trace Metal Sorption to Estuarine Suspended Particulate Matter. *Chemosphere* **1996,** *33* (6), 1027–1040.

19.   McKay, G.; Allen, S.J. Surface Mass-Transfer Processes Using Peak as an Adsorbent for Dyestuffs. *Can. J. Chem. Eng.* **1980,** *58* (4), 521–526.

20.   McKay, G.; Allen, S.J. Single Resistance Mass Transfer Models for Adsorption of Dyes on Peat. *J. Sep. Process Technol.* **1983,** *4*, 1–7.

21.   Baybars, A.F.; Yilmaz, M.T.; Bayar, S.; Elkoca, M.T. Investigation of Adsorption of the Dyestuff Astrazon Red Violet 3RN (Basic Violet 16) on Montmorillonite Clay. *Braz. J. Chem. Eng.* **2014,** *31* (1), 171–182.

22.   Alfaro-Cuevas-Villaneuva, R.; Hidalgo-Vasquez, A.R.; Penagos, C.J.C.; Cortes-Martinez, R. Thermodynamic, Kinetic, and Equilibrium Parameters for the Removal of Lead and Cadmium from Aqueous Solutions with Calcium Alginate Beads. *Sci. World J.* [Online] **2014,** Article 647512. http://dx.doi.org/10.1155/2014/647512 (accessed 13 March 2017).

23.   Biggs, K.B.; Camden, J.P.; Anker, J.N.; Van Duyne, R.P. Surface-Enhanced Raman Spectroscopy of Benzenethiol Adsorbed from the Gas Phase onto Silver Film over Nanosphere Surfaces: Determination of the Sticking Probability and Detection Limit Time. *J. Phys. Chem. A* **2009,** *113* (16), 4581–4586.

24.   Whelan, C.M.; Smyth, M.R.; Barnes, C.J. HREELS, XPS, and Electrochemical Study of Benzenethiol Adsorption on Au(111). *Langmuir* **1999,** *15* (1), 116–126.

25.   Hahner, G.; Woll, C.; Buck, M.; Grunze, M. Investigation of Intermediate Steps in the Self-Assembly of *N*-Alkanethiols on Gold Surfaces by Soft X-Ray Spectroscopy. *Langmuir* **1993,** *9* (3), 1955–1958.

26.   Schreiber, F.; Eberhardt, A.; Leung, T.Y.B.; Schwartz, P.; Wetterer, S.M.; Lavrich, D.J.; Berman, L.; Fenter, P.; Eisenberger, P.; Scoles, G. Adsorption Mechanisms, Structures, and Growth Regimes of an Archetypal Self-Assembling System: Decanethiol on Au(111). *Phys. Rev. B* **1998,** *57* (19), 12476–12481.

27.   Carron, K.T.; Hurley, L.G. Axial and Azimuthal Angle Determination with Surface-Enhanced Raman Spectroscopy: Thiophenol on Copper, Silver, and Gold Metal Surfaces. *J. Phys. Chem.* **1991,** *95* (24), 9979–9984.

ACRONYMS AND ABBREVIATIONS

α	catalyst ratio
α_{zz}	tensor value of first-order Langmuir kinetics
β	$(1 + \alpha)\, I_{max}$
ΔE_{12}	$E_2 - E_1$
ΔE_{13}	$E_3 - E_1$
ΔE_{23}	$E_3 - E_2$
a	mass rate diffusion rate or LDF effective mass transfer coefficient
a_1	fraction of site
a_e	initial adsorption rate
b	constant with $b < 1$
b_e	desorption constant
Cons.	consecutive (in-series) rate model
C_d	zero when diffusion is limiting step
DEM	double exponential rate model
E_1, E_2, and E_3	activation energies associated with rate constants k_1, k_2, and k_3, respectively
f	function
I	intensity
I_{max}	experimental maximum intensity
I_{maxp}	predicted maximum intensity
I_{min}	experimental minimum intensity
k	rate constant
k_d	rate of intraparticle diffusion-controlled adsorption constant
k_f	film diffusion constant
k_{obs}	observed (effective) rate constant
LDF	linear driving force
n	constant
pH	potential of hydrogen
R	ideal gas constant
R_{adj}	adjusted I_{max} intensity factor
R_{exp}	experimental relative intensity, based on the experimental maximum intensity
R_p	predicted relative intensity, based on the predicted maximum intensity, I_{maxp}
S	site type
SERS	surface-enhanced Raman spectroscopy
T	temperature
t	time
t_{50}	time when the reaction reaches a relative intensity of 0.5 ($R_p = 0.5$), or the time when the reaction reaches 50% conversion
URMS	Universal Rate Model Selector

DISTRIBUTION LIST

The following individuals and organizations were provided with one Adobe portable document format (pdf) electronic version of this report:

U.S. Army Edgewood Chemical
Biological Center (ECBC)
Spectroscopy Branch
RDCB-DRI-S
ATTN: Maswadeh, W.
  Vanderbeek, R.
  Moon, R.
  Tripathi, A.

Defense Threat Reduction Agency
J9-CBS
ATTN: Graziano, A.

Department of Homeland Security
RDCB-PI-CSAC
ATTN: Negron, A.
DHS-S&T-RDP-CSAC
ATTN: Strang, P.

Defense Technical Information Center
ATTN: DTIC OA

G-3 History Office
U.S. Army RDECOM
ATTN: Smart, J.

ECBC Technical Library
RDCB-DRB-BL
ATTN: Foppiano, S.
  Stein, J.

Office of the Chief Counsel
AMSRD-CC
ATTN: Upchurch, V.

ECBC Rock Island
RDCB-DES
ATTN: Lee, K.
RDCB-DEM
ATTN: Grodecki, J.

EDGEWOOD CHEMICAL BIOLOGICAL CENTER

A U.S. Army RDECOM Laboratory